Available online at www.sciencedirect.com
ScienceDirect
International Journal of Heat and Fluid Flow 29 (2008) 281–291
International Journal of HEAT AND FLUID FLOW
www.elsevier.com/locate/ijhff

Effect of non-local equilibrium on minimal thermal resistance porous layered systems

Geneviève Leblond, Louis Gosselin *

Département de Génie Mécanique, Université Laval, Québec, Québec, Canada G1K 7P4

Received 17 August 2006; received in revised form 22 June 2007; accepted 26 June 2007
Available online 9 August 2007

Abstract

In this paper, the cooling of a heat-generating surface by a stacking of porous media (e.g., metallic foam) through which fluid flows parallel to the surface is considered. A two-temperature model is proposed to account for non-local thermal equilibrium (non-LTE). A scale analysis is performed to determine temperatures profiles in the boundary layer regime. The hot spot temperature is minimized with respect to the three design variables of each layer: porosity, pore diameter, and material. Global cost and mass are constrained. The optimization is performed with a hybrid genetic algorithm (GA) including local search to enhance convergence and repeatability. Results demonstrate that the optimized stacks do not operate in LTE. Therefore, we show that assuming LTE might result in underestimation of the hot spot temperature, and into different final designs as well.
© 2007 Elsevier Inc. All rights reserved.

Keywords: Optimization with genetic algorithms; Layered structure; Porous media; Cooling of electronics; Heat sink; Cold plate

1. Introduction

The potential of porous structures (e.g., metallic foam) in heat transfer systems is currently undergoing growing interest due to their large surface area per unit of volume. For example, Jeng et al. (2001) investigated the performance of a channel filled with metallic foam for electronic cooling applications. Jeng and Tzeng (2005) studied the performance of a heat sink made of aluminum foam with impinging jets, and obtained a thermal resistance 30% smaller than the one of traditional heat sink of similar size. Lage et al. (1996) introduced a porous layer in a cold plate used in radar systems. Compact heat exchangers with metal foam have been studied by Boomsma et al. (2003a,b) and Boomsma and Poulikakos (2001). The use of porous structures in heat exchangers has also been studied by Tadrist et al. (2004).

The difficulty in modeling heat and fluid flow within porous structures is due to the complexity of the flow as it proceeds through the intricate network of pores and capillaries. Even though Boomsma et al. (2003a) modeled the flow through the metal foam using periodic boundary conditions, one usually relies on spatially averaged quantities and effective properties to do so. The characterization of metallic foams for determining its effective properties is therefore an active field (Giani et al., 2005; Crittenden and Cole, 2005). Boomsma and Poulikakos (2001) showed that despite of a high foam porosity, the overall effective thermal conductivity of a foam heat exchanger is governed by the solid phase. They derived some expressions for the foam effective conductivity.

When used as thermal enhancers, porous structures are designable to some extent (Bejan, 2004a) just as the shape of fins can be varied for maximizing its performance (Bobaru and Rachakonda, 2004; Jany and Bejan, 1998). The design variables include in particular the pore network structure, pore sizes, solid materials, and porosities. Boomsma et al. (2003b) investigated experimentally the effect of

* Corresponding author. Tel.: +1 418 656 7829; fax: +1 418 656 7415.
E-mail address: Louis.Gosselin@gmc.ulaval.ca (L. Gosselin).

0142-727X/$ - see front matter © 2007 Elsevier Inc. All rights reserved.
doi:10.1016/j.ijheatfluidflow.2007.06.007

Nomenclature

a_{sf}	interfacial surface area per unit volume, $m^2\ m^{-3}$
Be	Bejan number
c_p	heat capacity, $J\ kg^{-1}\ K^{-1}$
c	cost per unit of mass, $\$\ kg^{-1}$
C	cost, \$
D	diameter of the pipes
h	interstitial heat transfer coefficient, $W\ m^{-2}\ K^{-1}$
k	thermal conductivity, $W\ m^{-1}\ K^{-1}$
K	permeability, m^2
L	length, m
M'	mass per unit of length, $kg\ m^{-1}$
N	number of layers in the y-direction
Nu	Nusselt number
P	pressure, Pa
q''	heat flux, $W\ m^{-2}$
S	number of cells in the x-direction
T	temperature, K
u	velocity, $m\ s^{-1}$
x, y	Cartesian coordinates, m

Greek symbols

α	thermal diffusivity, $m^2\ s^{-1}$
Δ	difference
ϕ	porosity
γ	penalty coefficient
μ	viscosity, $kg\ m^{-1}\ s^{-1}$
ρ	density, $kg\ m^{-3}$

Subscripts

eff	effective
f	fluid
j	layer index
s	solid
w	wall
0	constraint value

Superscript

$\sim$	dimensionnless quantity

compression applied to the porous structure on the overall performance and found that with the same required pumping power, compressed metallic foam heat exchangers generated thermal resistances that were 2–3 times lower than the best commercially available heat exchanger tested. Wildi-Tremblay and Gosselin (2007) minimized the hot spot temperature of a porous layered stacking varying the porosity and materials, assuming local thermal equilibrium (LTE).

The consideration of non-local thermal equilibrium in porous media modeling has gained more attention in the past years (Amiri and Vafai, 1994; Jiang et al., 1999; Lee and Vafai, 1999; Jiang and Ren, 2001; etc). Amiri et al. (1995) thoroughly studied the effect of various flows, of thermal dispersion, of variable porosity and of different boundary conditions on the thermal response of a porous structure submitted to forced convection using a two-equation model. Jiang et al. (1999) compared numerical and experimental results using both the LTE and non-LTE assumptions for a porous media composed with glass packed beds while considering thermal dispersion. They observed that the thermal equilibrium model was inadequate in the case of water flow in metallic porous media.

In this paper, we use a two-temperature model for optimizing the solid materials, porosities, as well as pore diameters in a stack of porous layers. The optimization of the pore diameters is not possible without considering non-LTE. The objective is to minimize the hot spot temperature under mass and cost constraints. The optimization is performed with a genetic algorithm (GA) confined with local search. The optimal designs are compared with those obtained assuming LTE in order to assess the influence of such an assumption of the final results.

2. Problem formulation and mathematical model

The geometry of the problem studied is depicted schematically in Fig. 1. The structure is composed of a stack of N porous layers at the base of which a constant heat flux q'' is applied. The top wall of the structure is assumed adiabatic. The heat is dissipated by conduction through the solid matrix and is brought out of the system by convection due to fluid flow in the pores. To each layer are assigned a material, a porosity ϕ and a pore diameter D. The porosity is defined as the ratio of the volume occupied by the fluid to the total volume of the layer. These three parameters will be optimized in order to minimize the hot spot temperature T_{max}. In Table 1, we list the four materials considered in the study, as well as their respective properties and cost. As several designs will be tested during the optimization process, the model on which we will rely for the evaluation

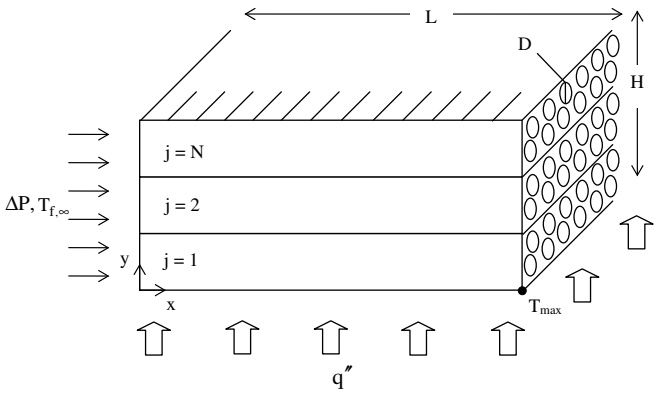

Fig. 1. Schematic diagram of the system.

Table 1
Properties (normalized to that of air at 300 K (Incropera and DeWitt, 2002)) and cost (normalized to that of iron (www.metalprices.com, as of October 26, 2005.)) of the considered materials

Material	$\tilde{\rho}$	$\tilde{k}$	$\tilde{c}$
Aluminum	2327.5	9011.4	8.9
Copper	7691.6	15 247.2	18.7
Iron	6776.3	3049.4	1
Brass	7344.6	4182.5	11.6

of the thermal performance of a design should be as simple as possible in order to limit the computational time.

The modeling of fluid flow through the sinuous paths of the porous structure requires various assumptions. A pile of pores of diameter D aligned in the flow direction axis was chosen to model the porous structure. It should be clear from that point that the porosity ϕ and the pore diameter D can be treated as independent design variables for the internal porous structure considered. For example, increasing the number of identical pores per unit of volume will increase ϕ but does not affect D. Similarly, two samples with the same porosity can have pores with different diameters. Other porous structures could be considered in future work resulting in different relationships between the thermofluid properties and internal porous structure. The procedures and ideas explored in this paper would still apply. The flow is considered unidirectional in the x-direction. It is the imposed pressure drop between the system inlet and outlet, ΔP, that is responsible for the fluid flow. The flow regime is assumed to be laminar, and Darcy's law (Bejan, 2004b) is used to determine the spatially averaged fluid velocity in the porous layers:

$$u_j = \frac{K_j \Delta P}{\mu L} \tag{1}$$

where K_j is the jth layer permeability and L, the system length (Fig. 1). The permeability K_j represents the material capability to let the fluid flow. For the porous architecture considered in the current study, the porosity–permeability relation is determined straightforwardly by calculating the mass flow rate generated in the pile of pores for a fixed pressure drop and comparing the result with Darcy law (Bejan, 2004b; Nield and Bejan, 1991), Eq. (1), leading to

$$K_j = \frac{\phi_j D^2}{32} \tag{2}$$

Because of the anisotropic arrangement of the solid and fluid phases in the porous medium, the following relation gives a fair approximation of the equivalent thermal conductivity (Pham and Torquato, 2003):

$$k = k_s \frac{(1-\phi)}{(1+\phi)} \tag{3}$$

which is justified by the fact that the solid conductivity is much larger than the one of the fluid. Eq. (3) gives the equivalent conductivity along the y-direction. In the x-direction, convection heat transfer prevails and thus, the thermal conductivity is neglected, which means that the local Peclet number should be larger than 1.

Finally, the viscous dissipation in the pores is considered negligible and the properties are assumed constant.

As mentioned in Section 1, we want to assess the importance of non-local thermal equilibrium within the porous structure. Therefore, a two-equation model is required to describe the problem as the temperature of the solid and fluid phases are different. Accounting for the above-mentioned simplifications, two energy equations were developed, one for T_s and one for T_f (Khashan et al., 2006):

$$\frac{\partial}{\partial y}\left(k_j \frac{\partial T_s}{\partial y}\right) + h a_{sf}(T_f - T_s) = 0 \tag{4}$$

$$(\rho c_p)_f \frac{\partial (u_j T_f)}{\partial x} = h a_{sf}(T_s - T_f) \tag{5}$$

where h and a_{sf} are respectively the pore internal heat transfer coefficient and the interfacial surface area per unit volume. For the porous geometry considered, it can be shown that

$$a_{sf} = \frac{4\phi}{D} \tag{6}$$

For convenience, the governing equations, Eqs. (4) and (5), were non-dimensionalized as follows:

$$\frac{\partial}{\partial \tilde{y}}\left[\tilde{k}_j \frac{(1-\phi)}{(1+\phi)} \frac{\partial \widetilde{T}_s}{\partial \tilde{y}}\right] + \frac{4Nu\phi}{\widetilde{D}^2}(\widetilde{T}_f - \widetilde{T}_s) = 0, \quad \text{in the solid phase} \tag{7}$$

$$Be \widetilde{K}_j \frac{\partial \widetilde{T}_f}{\partial \tilde{x}} = \frac{4Nu\phi}{\widetilde{D}^2}(\widetilde{T}_s - \widetilde{T}_f), \quad \text{in the fluid phase} \tag{8}$$

using the dimensionless variables

$$\tilde{x}, \tilde{y} = \frac{x, y}{L}, \quad \widetilde{T}_s, \widetilde{T}_f = \frac{(T_s, T_f) - T_0}{q'' L / k_f}, \quad \widetilde{K}_j = \frac{K_j}{L^2} = \frac{\phi \widetilde{D}^2}{32} \tag{9}$$

$$Be = \frac{L^2 \Delta P}{\alpha_f \mu}, \quad \tilde{k} = \frac{k_s}{k_f}, \quad Nu = \frac{hD}{k_f} \tag{10}$$

In the above equations, Be and Nu are the Bejan and Nusselt numbers, respectively. For most of the results presented in the paper, Nu was set to 3.66 (Çengel, 2003). This value corresponds to the Nusselt number for thermally fully developed flow within a tube subject to constant surface temperature. In the present case, we have neither a fixed surface temperature nor a fixed heat flux on the pore surface. However, it is common practice in similar situation to use a number of order 4 for Nu as an approximation, hence $Nu = 3.66 \sim 4$ (Bejan, 2004b, 2000; Çengel, 2003; Incropera and DeWitt, 2002). The numerical solving of Eqs. (7) and (8) will result in a temperature distribution for each of the solid and fluid phases. A unique solution will be obtained using the boundary conditions

$$\widetilde{T}_f(0,\tilde{y}) = 0, \quad \tilde{k}\left(\frac{1-\phi}{1+\phi}\right)\frac{\partial \widetilde{T}_s}{\partial \tilde{y}} = -1 \quad \text{at } \tilde{y} = 0,$$

$$\frac{\partial \widetilde{T}_s}{\partial \tilde{y}} = 0 \quad \text{at } \tilde{y} = \widetilde{H} \tag{11}$$

The minimization of $\widetilde{T}_{max}$ will be performed under global mass and cost constraints. Only the mass of the solid phase needs to be taken into account when evaluating the global mass of the stacking as the density of the air is much smaller than the one of the solid phase materials, Table 1. In other words, the actual mass $\widetilde{M}$ of the heat sink is the summation of the mass of the solid phase of each porous layer. The value of $\widetilde{M}$ must be equal or smaller than a specified value $\widetilde{M}_0$ that we do not want to exceed,

$$\widetilde{M} = \frac{M'}{\rho_f L^2} = \sum_{j=1}^{N} \tilde{\rho}_j(1-\phi_j)\Delta\tilde{y}_j \leqslant \widetilde{M}_0 \tag{12}$$

where $\Delta\tilde{y}_j$ is the thickness of the jth layer. It is also possible to consider a total cost constraint, which is the summation of the price associated with each layer,

$$\widetilde{C} = \sum_{j=1}^{N} \tilde{\rho}_j\tilde{c}_j(1-\phi_j)\Delta\tilde{y}_j \leqslant \widetilde{C}_0 \tag{13}$$

where $\tilde{c}_j$ is the relative price per unit mass. The values of $\tilde{c}_j$ for the four materials considered in this study are reported in Table 1. In Eq. (13), $\widetilde{C}_0$ is the threshold value of the total price that we do not want to exceed.

3. Numerical calculation of heat and fluid flow

The calculation domain is divided into quadrilateral control volumes uniformly distributed over the entire domain and at the center of each sits a grid point. The integration of the coupled non-dimensionalized differential equations, Eqs. (7) and (8), is performed on these control volumes to obtain the solid and fluid temperatures (T_s, T_f) at each node. The grid is made of N_x cells in the axial direction, i.e. N_x cells per unit length along the x-direction, and of $\widetilde{H}N_x$ cells in the y-direction so that the cell density is the same in both directions. As pointed out earlier, all the cells that compose a physical layer share the same properties $(\phi, \tilde{\rho}, \tilde{k})$. At the boundaries of the domain, the nodes are located directly on the boundary, resulting in half-sized control volumes.

The dimensionless governing equations were discretized through the application of the finite volume method (Patankar, 1980). An upwind differencing scheme was used to discretize the convective term. Linear interpolation functions for the temperature between consecutive grid points were assumed for the conductive term discretization. In order to accurately handle the abrupt changes of the thermal conductivity encountered when successive layers are made of different materials, the harmonic mean was chosen to define the equivalent thermal conductivity at the control volume interfaces. The discretization results in two coupled systems of equations: one for $\widetilde{T}_s$ and one for $\widetilde{T}_f$. A column-by-column approach is used to solve the equations, resulting in a diagonal matrix for $\widetilde{T}_f$ and a tridiagonal matrix for $\widetilde{T}_s$ at each column (x-position) of the domain. Starting with an initial guess and sweeping from left to right, we first evaluate the fluid temperature in a column of cells. The obtained values for $\widetilde{T}_f$ are used to determine the solid temperatures of the column in consideration. These fluid and solid temperatures then contribute to the resolution of the temperatures in the next column. Sweepings of the domain continue until convergence. In this paper, convergence is declared when the relative difference between the maximal temperature and that from the previous iteration becomes smaller than 10^{-6}. To foster convergence, over-relaxation was included in the algorithm.

A mesh independence study is necessary to ensure the accuracy of the results. The maximal temperature is first found for a relatively small value of N_x. N_x is then doubled and $\widetilde{T}_{max}$ is recalculated. The mesh refinement goes on until further mesh density doubling results in a $\widetilde{T}_{max}$ variation smaller than 1%. We concluded that for a porosity of 0.5, 60 control volumes per length unit are sufficient to describe well the problem when $10^{11} \leqslant Be \leqslant 10^{13}$. Moreover, it was observed that a larger porosity requires more control volumes per unit length. In fact, when the porosity is set equal to 0.9, 60, 120 and 240 are needed for respective Bejan numbers of 10^{11}, 10^{12} and 10^{13}. As the porosities will vary during the optimization process, we selected the large mesh density obtained with large porosity values.

4. Scaling analysis and validation

In order to validate the numerical model presented above, we developed scaling equations for the solid and fluid temperatures evaluated at the wall in the thermal boundary layer regime. The integral method was used; the dimensionless governing equations were integrated from $\tilde{y} = 0$ to $\tilde{y} = \tilde{\delta}$, the thickness of the thermal boundary layer. Integrating the first term of Eq. (7) yields

$$\int_0^{\tilde{\delta}} \frac{\partial}{\partial \tilde{y}}\left[\tilde{k}\frac{(1-\phi)}{(1+\phi)}\frac{\partial \widetilde{T}_s}{\partial \tilde{y}}\right] d\tilde{y} = 1 \tag{14}$$

where the boundary conditions, Eq. (11), have been invoked. Therefore, the integration of the second term of Eq. (7) results in

$$\int_0^{\tilde{\delta}} \frac{4Nu\phi}{\widetilde{D}^2}(\widetilde{T}_f - \widetilde{T}_s)\, d\tilde{y} = -1 \tag{15}$$

Finally, the integration of Eq. (8) along with Eq. (15) means that:

$$\int_0^{\tilde{\delta}} Be\widetilde{K}\frac{\partial \widetilde{T}_f}{\partial \tilde{x}}\, d\tilde{y} = 1 \tag{16}$$

The integral method requires that we specify a realistic temperature profile in the thermal boundary layer. In this paper, we assumed linear temperature profiles:

$$\widetilde{T}_{\mathrm{f}}(\tilde{x},\tilde{y}) = \widetilde{T}_{\mathrm{f,w}}(\tilde{x})(1-\hat{y}), \quad \tilde{y} < 1 \tag{17}$$

$$\widetilde{T}_{\mathrm{s}}(\tilde{x},\tilde{y}) = \widetilde{T}_{\mathrm{s,w}}(\tilde{x})(1-\hat{y}), \quad \tilde{y} < 1 \tag{18}$$

where the subscript w stands for wall, and

$$\hat{y} = \frac{\tilde{y}}{\tilde{\delta}} \tag{19}$$

Using Eq. (17) and the heated wall boundary condition, we find that the solid wall temperature can be expressed as

$$\widetilde{T}_{\mathrm{s,w}} = \frac{\tilde{\delta}}{\tilde{k}^*}, \tag{20}$$

where $\tilde{k}^*$ denotes $\tilde{k}(1-\phi)/(1+\phi)$. The appraisal of Eqs. (15) and (16), with the application of Eqs. (17)–(20), gives an approximation of the thermal boundary layer thickness as well as of the solid and fluid wall temperatures:

$$\tilde{\delta}(\tilde{x}) = \left(\frac{2\tilde{k}^*\tilde{x}}{Be\widetilde{K}}\right)^{1/2} \tag{21}$$

$$\widetilde{T}_{\mathrm{s,w}} = \left(\frac{2\tilde{x}}{Be\widetilde{K}\tilde{k}^*}\right)^{1/2} \tag{22}$$

$$\widetilde{T}_{\mathrm{f,w}} = \left(\frac{2\tilde{x}}{Be\widetilde{K}\tilde{k}^*}\right)^{1/2} - \frac{\widetilde{D}^2}{2Nu\phi}\left(\frac{Be\widetilde{K}}{2\tilde{k}^*\tilde{x}}\right)^{1/2} \tag{23}$$

It is worth noting that the second term of Eq. (23) represents the difference between $\widetilde{T}_{\mathrm{s,w}}$ and $\widetilde{T}_{\mathrm{f,w}}$. It is negligible when local thermal equilibrium applies. This scaling analysis reveals that non-LTE prevails when $\widetilde{D}$ is large and when Nu is small.

In order to determine the range of validity of our model, we begin by relating the Bejan number to the local Reynolds number in the pore and fluid Prandtl number,

$$Re = \frac{UD}{\nu}, \quad \mathrm{Pr_f} = \frac{\nu}{\alpha_{\mathrm{f}}} \tag{24}$$

In Eq. (24), U is the local velocity in a pore. We can relate it to Darcy's spatially averaged fluid velocity: $U = u/\phi$. Combining Eq. (24) with Eqs. (9) and (10), we obtain:

$$Re = Be\frac{\widetilde{D}^3}{32\mathrm{Pr_f}} \tag{25}$$

For assuring the validity of our model, the flow in the pores needs to stay laminar, which translates in $Re < 2300$ (Bejan, 2004b). With $Pr_{\mathrm{f}} \sim 0.7$ (air) and $\widetilde{D} = 10^{-3}$, this leads to an upper limit for the Bejan number, i.e. $Be < 5\times10^{13}$. Most of our simulation were performed with $Be = 10^{11}$ (i.e., $Re \sim 4.5 \sim O(1)$). It is common to say that for Darcy law to apply, the local Re should be of order 1 or smaller, which is the case for most of our calculations. For $Re > O(1)$, Forchheimer flow usually prevails. In Forchheimer regime, there is an additional contribution to the total pressure drop (form drag due to solid obstacles) but the Darcy–Forchheimer transition is smooth (Nield and Bejan, 1991). However, with the porous structure considered here (pores aligned in the direction of the flow), this additional effect is clearly negligible as no "obstacle" is encountered by the flow. Therefore, the range of validity of Darcy law extends above $Re \sim O(1)$, because of the "special" internal structure of this porous medium. This is why more elaborate models are not required, as long as $Be < 5\times10^{13}$. The lower limit in terms of Be for the model validity is imposed by the requirement of a fully developed flow within the pores. In terms of our dimensionless variables, the entry zone length is small compared to L when (Bejan, 2004b, Chapter 3),

$$\widetilde{L}_{\mathrm{entry}} \sim 0.05Re\mathrm{Pr}\widetilde{D} \ll 1 \tag{26}$$

or

$$\widetilde{L}_{\mathrm{entry}} \sim 10^{-3}Be\widetilde{D}^4 \ll 1 \tag{27}$$

Therefore, for the model to be valid, the scale analysis shows that $\widetilde{D}$ has to be smaller than ~0.01, 0.006 and 0.003 for Bejan numbers of 10^{11}, 10^{12} and 10^{13}, respectively. It could be shown that these limiting values are the same as that for obtaining a laminar flow in the pores in an order of magnitude sense.

We validated our numerical model with the scale analysis presented above. A one-layer aluminum structure with $\phi = 0.5$, $\widetilde{D} = 0.001$ and $Be = 10^{11}$–10^{13} was used for the validation test. The value of $\widetilde{H}$ was increased to 5 in order to obtain a temperature value inferior to 1% of the hot spot temperature in the upper right corner (boundary layer regime). The solid and fluid temperatures were calculated with the numerical model presented in Section 3. We plotted both solid and fluid numerical temperatures evaluated at the heated wall as a function of $\tilde{x}^{1/2}$ for different Bejan numbers (Fig. 2). The values of the fitting curve slopes obtained numerically (0.0005, 0.0002 and 0.00005 for both solid and fluid phases, for Bejan numbers of 10^{11}, 10^{12} and 10^{13}, respectively) are of the same order of magnitude as the ones obtained analytically with Eqs. (22) and (23) (0.0007, 0.0002 and 0.00005 for the solid phase and 0.0007, 0.0002 and 0.00006 for the fluid phase).

From Eqs. (9), (22) and (23), we deduce that the difference between the solid and fluid temperatures at the wall of a thermal boundary layer (thermal boundary layer regime) is proportional to $\widetilde{D}^3$. Numerical results of $\widetilde{T}_{\mathrm{s,w,max}} - \widetilde{T}_{\mathrm{f,w,max}}$ as a function of $\widetilde{D}^3$ for $Be = 10^{11}$ displayed in Fig. 3 support our scale analysis.

Another validation test can be done by comparing the numerical maximal temperature in a boundary layer regime with the one defined by Eq. (22). By analyzing the latter, we observe that $\widetilde{T}_{\mathrm{s,w,max}}$ is obtained when $\tilde{x} = 1$. Furthermore, one would expect the hot spot temperature to be proportional to $(Be\widetilde{K}\tilde{k}^*)^{-1/2}$ with a coefficient of proportionality of order 1. The numerical results displayed in Fig. 4 are in excellent agreement with the analysis as we obtain a value of 1.1211 for the coefficient of proportionality.

Finally, from Eqs. (7) and (8), we anticipate to observe local thermal equilibrium if the pore internal Nusselt number was largely increased. In that limit, $\widetilde{T}_{\mathrm{s}}$ and $\widetilde{T}_{\mathrm{f}}$ should be equal. We compared the maximal temperature found for

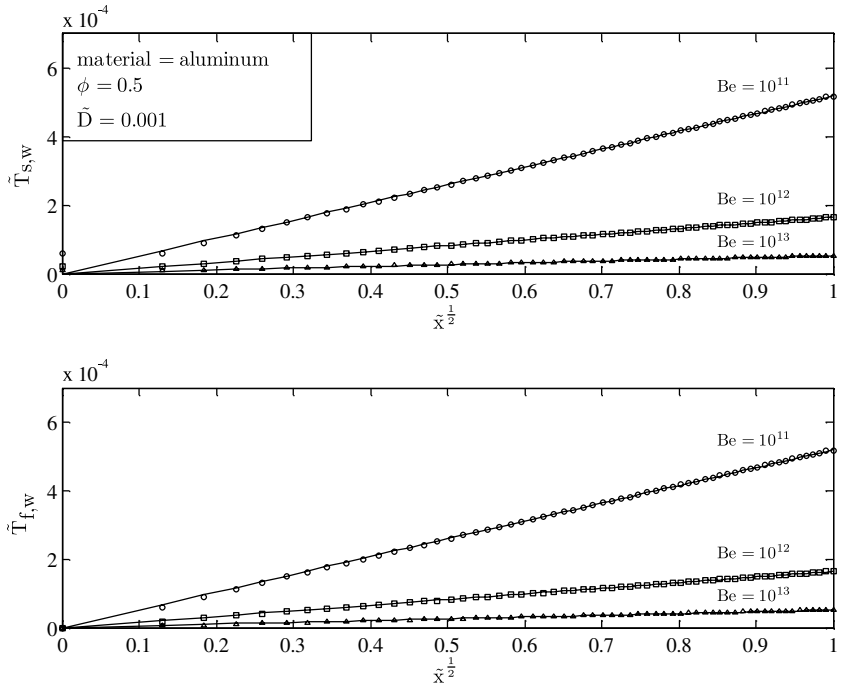

Fig. 2. Solid and fluid temperature at the heated wall for various Bejan numbers (boundary layer regime).

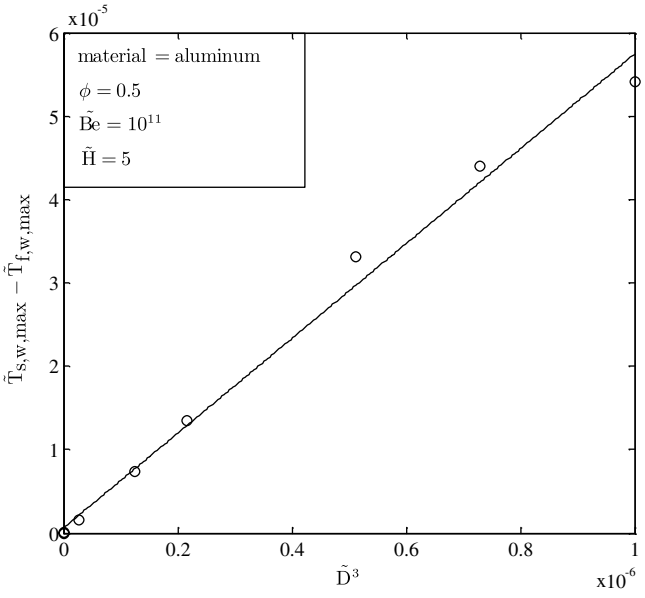

Fig. 3. Numerical solid-to-fluid temperature difference for various values of $\tilde{D}^3$ (boundary layer regime).

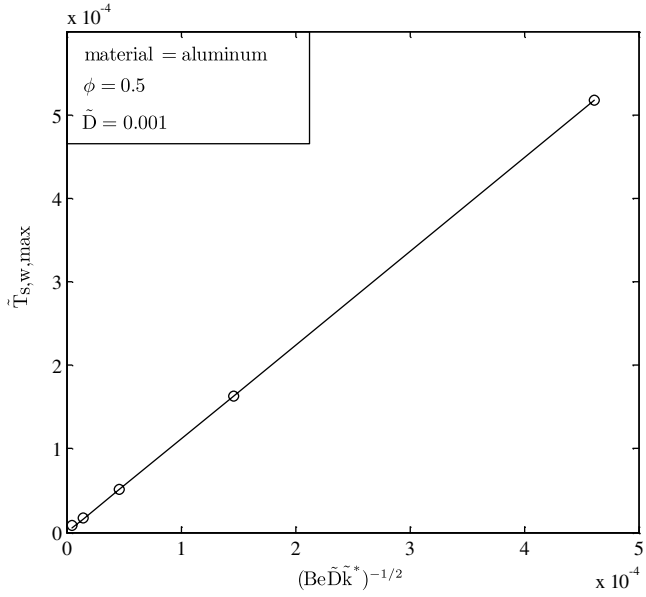

Fig. 4. Numerical maximal solid temperature at the heated wall for various Bejan numbers (boundary layer regime).

large *Nu* with the one obtained by Wildi-Tremblay and Gosselin (2007) who considered the LTE assumption to solve a problem similar to the one detailed in this paper. Note that this increase of *Nu* is a numerical artifact to validate the code. *Nu* could be increased in the turbulent regime, but then the fluid flow calculations would have to be adapted. Using one layer of aluminum with $\phi = 0.5$, $Be = 10^{11}$, $\widetilde{H} = 1$ and $\widetilde{D} = 0.009$, we found a relative difference inferior to 1% between Wildi-Tremblay and Gosselin's maximal temperature value and our $\widetilde{T}_{s,\max}$ as the Nusselt number reaches a value of 350. For these parameters, the relative difference between $\widetilde{T}_{s,\max}$ and $\widetilde{T}_{f,\max}$ is as well within a 1% range.

5. Optimization procedure

In the previous sections, we presented how we numerically evaluate the solid and fluid temperatures in a porous layered domain for a given set of parameters. In this part of the paper, we give a brief description of the optimization

toolbox based on genetic algorithms (GA), that will be used to optimize the architecture of the structure, i.e. minimize the hot spot temperature while considering mass and cost constraints. For a more detailed explanation about the toolbox, consult Renner and Ekárt (2003).

The GA starts by randomly producing the designs (i.e., chromosomes) of the initial population. In this paper, the initial population is made of 20 individuals. Each design is defined by a set of $3N$ parameters, N being the number of layers of the porous structure. The porosity ϕ, the dimensionless diameter $\widetilde{D}$ and the material correspond to the three design variables per layer considered in the present study. To attain sufficient precision, we coded ϕ, $\widetilde{D}$ and the material with 4, 4 and 3 bits, respectively. Three bits were used to code the material to include the possibility (added to the four possibilities associated with the four materials considered) for the GA to assign "void" to a layer. Based on the fitness of each individual of the initial population, a stochastic universal sampling strategy (SUS) is then employed to determine which designs will "reproduce" to yield the next generations. The following function F is the actual objective function that is used for the optimization in order to take into account the mass and cost constraints:

$$F = \frac{\widetilde{T}_{\max}}{(Be\widetilde{D}_{\text{opt}}^2)^{-1/2}} + \gamma_M \max\left[\left(\frac{\widetilde{M}-\widetilde{M}_0}{\widetilde{M}_0}\right),0\right] + \gamma_C \max\left[\left(\frac{\widetilde{C}-\widetilde{C}_0}{\widetilde{C}_0}\right),0\right], \tag{28}$$

where $\widetilde{D}_{\text{opt}}$ is the optimal dimensionless diameter (for details of its value determination, see Section 6), and γ_M and γ_C are the penalty coefficients set equal to 1. All three terms of Eq. (28) are of order 1 so that the GA is more likely to properly reject the designs that do not respect the constraints. The hot spot temperature is normalized with $(Be\widetilde{D}_{\text{opt}}^2)^{-1/2}$, the scale of $\widetilde{T}_{\text{s,max}}$ in the thermal boundary layer regime. From the optimization toolbox processes of crossover and mutation performed on the selected individuals, new designs arise. (In this paper, we used 2 crossover points and a probability of 0.05 for mutation to take place.) Reinsertion of these new designs in the population is then executed based on an elitist strategy, i.e. the 4 best designs of the previous population are ensure to propagate in the next generation. This new population then becomes the initial one for the next generation, and so on until convergence is reached. The criterion chosen to declare convergence is when 300 consecutive generations do not show any improvement in $\widetilde{T}_{\text{s,max}}$.

Measures were taken to improve the GA convergence rate. A really effective one is the creation of a database as the GA runs to prevent it from recalculating the objective value of designs that have already been generated earlier in the algorithm. Furthermore, local search was introduced in the algorithm. In the present study, it is performed on all individuals at every 10 generations. For each design, the performance of two neighboring designs is calculated, and the fittest individual among the actual design and its two neighbors is reintroduced in the population. To determine the first neighbor, a certain number of design variables (porosities and/or diameters) are randomly chosen. Then, the value of each of these design variables is replaced randomly by the closest upper or lower value for this design variable. This procedure defines a direction in the design space from the actual design to the first neighbor. The second neighbor is the design located in the opposite direction in the design space.

6. Optimization of the pore diameters

Before optimizing the stacking with respect to the porosities and materials, we measured the effect of the pore diameter $\widetilde{D}$ on the hot spot temperature obtained with the numerical code described in Section 3. The analysis was performed for a one-layer structure of porosity ϕ set equal to 0.5 for Bejan numbers between 10^{11} and 10^{13}. Fig. 5 displays the effect of the pore diameter on $\widetilde{T}_{\text{s,max}}$ for the case of aluminum, $Be = 10^{11}$. The figure clearly shows that there is an optimal value of $\widetilde{D}$ that leads to a minimal hot spot temperature (indicated by a small white circle in Fig. 5). This could have been anticipated. Looking at the solid phase dimensionless governing equation (7), we realize that a larger diameter means a higher fluid flow velocity but a smaller heat transfer coefficient. Thus, there is a tradeoff $\widetilde{D}$-value for the cooling to be as efficient as possible. The values of $\widetilde{D}_{\text{opt}}$ obtained numerically with $\phi = 0.5$ (aluminum) are 0.0085, 0.005 and 0.003 for respective Bejan numbers of 10^{11}, 10^{12} and 10^{13}. It should be pointed out that for given parameters, the optimal diameter, $\widetilde{D}_{\text{opt}}$, does not yield local thermal equilibrium. In other

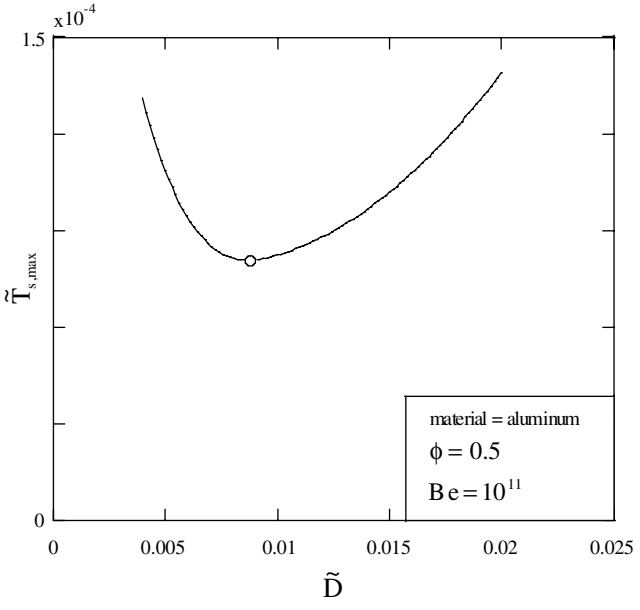

Fig. 5. Hot spot temperature for various values of the pore diameter.

words, optimal porous layered stacking does not operate with LTE. Since the value of $\widetilde{D}$ is a design parameter in the GA, we would expect the GA to generate designs having $\widetilde{D}$ close to the $\widetilde{D}_{\text{opt}}$ found here for given Be and porosity. Therefore, local thermal equilibrium should not be encountered after the optimization is performed.

7. Optimal stacking with and without constraints

In this section of the paper, the GA was used to optimize a layered structure submitted to various mass and cost constraints. GAs rely in part on probabilistic processes, and therefore, two optimization runs with the exact same settings can potentially lead to different final results. To measure the repeatability of the results, four different simulations were performed for each set of constraints. A stacking of three layers was chosen to execute the optimization. Considering the number of bits associated with each design variable (Section 5), this means that there are about 10^9 possible designs. The GA allowed us to optimize the system by evaluating only a small fraction of these designs. The optimal designs generated with $Be = 10^{11}$ and $\widetilde{H} = 0.25$ are presented in Table 2.

In Table 2, # is the design number, G is the generation in which the optimal design appeared in each of the 4 runs, the subscript m refers to the minimized hot spot temperature and $d_{\text{s–f}}$ consists in the relative difference between the maximal solid and fluid temperatures. The latter is calculated as follows:

$$d_{\text{s–f}} = \frac{\widetilde{T}_{\text{s,max,m}} - \widetilde{T}_{\text{f,max,m}}}{\widetilde{T}_{\text{f,max,m}}} \tag{29}$$

The repeatability of the results greatly stands out from Table 2. In fact, for 4 of the 5 sets of constraints considered in the study, the same optimal design was generated for the four simulations realized. This is likely due to the relatively small size of the chromosomes describing each individual, to the use of local search as well as to the limited design space. Perfect repeatability is not met though for the cost-constrained optimizations for which two different designs were generated (#4a and #4b). Nevertheless the thermal performances of the designs found in that case vary only slightly. There is less than 5% of relative difference between the hot spot temperatures of the two designs found by the GA. The one having the highest $\widetilde{T}_{\text{s,max,m}}$ (#4b, 10.054×10^{-5}) obviously does not correspond to the global optimum for the specified parameters, i.e. the GA got trapped in a local minimum. Other methods, the so-called niching methods, exist to prevent the population from converging too early to some local optimum (Renner and Ekárt, 2003). A classification and a discussion of some of these are presented in Mahfoud (1995). Local search and the use of a database (Section 5) definitely helped the convergence to be achieved faster. In 80% of the simulations performed and described in Table 2, it took less than 50 generations for the GA to find the optimal design, which means that less than 10^{-5}% of the possible designs were evaluated.

As shown from the last column of Table 2, the designs generated by the genetic algorithm do not yield LTE. Indeed, the values of $d_{\text{s–f}}$, used here as a thermal equilibrium indicator, are quite far from zero. This result was expected given the conclusion of the study on the effect of the size of the pore diameter $\widetilde{D}$ on the hot spot temperature. From that study (Section 6), we obtained numerical

Table 2
Parameters of the fittest designs found by the GA for five sets of mass and cost constraints (non-LTE)

Constraints		#	G	Configuration of the jth layer (material, Φ, $\widetilde{D}$)			$\widetilde{M}$	$\widetilde{C}$	$\widetilde{T}_{\text{s,max,m}} \times 10^5$	$d_{\text{s–f}}$ (%)
$\widetilde{M}_0$	$\widetilde{C}_0$			1	2	3				
N/A	N/A	1	18,19,29,46	Cu 0.5625 0.00868	Cu 0.6875 0.00802	Cu 0.8750 0.00802	562	10515	7.8752	112
140	N/A	2	69,32,41,28	Al 0.6250 0.00868	Al 0.7500 0.00802	Al 0.9375 0.00802	134	1190.6	9.7361	108
50	N/A	3	27,11,14,26	Al 0.8125 0.00868	Al 0.9375 0.00802	Void	48.1	427.7	12.642	107
N/A	1300	4a	31,38	Al 0.6250 0.00868	Al 0.7500 0.00802	Al 0.8750 0.00802	146	1294.7	9.5865	107
		4b	25,28	Al 0.6250 0.00868	Fe 0.5000 0.00802	Al 0.8125 0.00802	408	1238.8	10.054	109
100	1000	5	91,31,28,69	Al 0.75 0.00868	Al 0.8125 0.00802	Al 0.9375 0.00736	97.4	866.97	10.593	106

values of the optimal pore diameter, $\widetilde{D}_{opt}$, for various Bejan numbers, porosities and materials. For $Be = 10^{11}$, we had found $\widetilde{D}_{opt} = 0.0085$ which is close to the value of 0.00868 assigned by the GA to the first layer of each optimized design. The following layers were all assigned pore diameters in the vicinity of $\widetilde{D}_{opt}$ as well. Another pattern deduced from Table 2 is the increase of the porosity ϕ as the layers are more distant from the heated wall. This is consistent with Bobaru and Rachakonda (2004) and Jany and Bejan (1998) where optimizations of a fin mass-constrained profile are performed. The resulting fins are thicker at the base and gradually thinner further from it. That means that more solid near the heat-generating wall provides a more efficient cooling.

Looking at the materials assigned by the GA in order to get the fittest designs presented in Table 2, we see that when it was not constrained, copper was attributed to each layer (#1). This was predictable since copper is the most conductive material among the ones considered in the study (see Table 1). When the GA had less freedom to morph, i.e. when mass and/or cost constraints limited the design space, the global optimum designs were all constituted with aluminum (#2, #3, #4a, and #5). That material represented a good tradeoff in that case between heat transfer, mass and cost features. We remark that for all cases, the GA closely satisfied the constraints (limit of constraints). For example, when the cost constraint of 1300 was imposed, the global mass achieved was 1294.7 (#4a). To respect the mass and cost constraints, we note that the GA assigned higher porosities. If changes in the porosity are not sufficient to meet constraints, the GA removes layers by attributing them a porosity of 1 (no solid material). By doing so, it indirectly optimizes the height of the stacking, additionally to the porosities, diameters and materials. This phenomenon was observed for the dramatically mass-constrained optimization (design # 3 in Table 2). To respect $\widetilde{M} \leqslant 50$ while minimizing the hot spot temperature, the GA took off the last layer. It should be pointed out that as constraints are imposed (less freedom to morph), the thermal performances of the optimal designs are reduced.

Table 3
Comparison of the hot spot temperatures of various designs considering either non-LTE or LTE

Design #	$\widetilde{T}_{max,m} \times 10^5$	
	Non-LTE	LTE
1	7.8752	5.2176
2	9.7361	6.7750
3	12.642	8.6416
4a	9.5865	6.7547
4b	10.054	7.1867
5	10.593	7.5814

8. Effect of non-local equilibrium

In this section of the paper, we used the results presented in Wildi-Tremblay and Gosselin (2007) to show the effect of non-LTE on the temperature distributions of a cooling system. We started by evaluating the hot spot temperature of the optimized designs listed in Table 2, this time using a model assuming local thermal equilibrium (LTE). In Table 3 are presented the resulting minimized hot spot temperatures as well as the ones obtained under non-LTE (obtained in Section 7). We observe from Table 3 that the hot spot temperature is smaller when local thermal equilibrium is assumed than when it is not. There is 40–50% of relative difference between the values obtained with LTE and the ones evaluated with non-LTE. In other words, assuming LTE will result in underestimating the hot spot temperature. This supports again the finding of the previous sections that optimal stacks operate far from LTE.

Even though the values of $\widetilde{T}_{max,m}$ varied significantly depending on whether LTE was assumed or not, we wanted to verify whether the design geometry optimized under LTE assumption would differ from the ones that we obtained when non-LTE was assumed (refer to Table 2). Therefore, we optimized with the GA a three-layer system with the

Table 4
Optimal designs obtained by the GA assuming LTE with $\widetilde{D} = 0.0085$ for various sets of constraints

Constraints		#	Configuration of the jth layer (material, ϕ)			$\widetilde{M}$	$\widetilde{C}$	$\widetilde{T}_{max,m} \times 10^5$
$\widetilde{M}_0$	$\widetilde{C}_0$		1	2	3			
N/A	N/A	1	Cu 0.058824	Cu 0.058824	Cu 0.35294	1628	30444	1.6567
140	N/A	2	Al 0.64706	Al 0.70588	Al 0.94118	138.1	1229.4	11.433
50	N/A	3	Al 0.88235	Al 0.94118	Al 0.94118	45.23	402.55	30.076
N/A	1300	4	Al 0.64706	Al 0.70588	Fe 0.70588	287.3	1291.6	10.829
100	1000	5	Al 0.76471	Al 0.82353	Al 0.94118	91.68	815.97	15.908

same constraint sets as previously, but this time assuming LTE. Under this assumption the diameter of the pore is non-designable (Wildi-Tremblay and Gosselin, 2007). Therefore, we imposed the optimal diameter found in Section 6 in every layer. The optimization results are reported in Table 4. We observe that the unconstrained problem (#1) leads to a low porosity design (and thus approximately three times heavier) compared with the one obtained previously (non-LTE). Similarly, the best design identified by the GA under the cost constraint (#4) considered was less porous and heavier than to the one in Table 2. On the other hand, the designs obtained with the mass constraints (#2, #3) and combined constraint (#5) were actually similar to the ones presented before. We conclude that for highly constrained problems, the designs identified by the GA with and without assuming LTE are similar (even though their predicted levels of performance differ), while the optimal design of less constrained problems is greatly influenced by the LTE assumption.

9. Conclusions

In this paper, we used a hybrid genetic algorithm to optimize a cooling system characterized by a stacking of porous layers through which a coolant fluid and at the base of which heat is generated. The objective was to minimize the hot spot temperature of the porous structure while facing different global constraints. The material, porosity and pore diameter of each layer represented the design variables. The pore diameter could be optimized for the porous structure considered as a two-equation model was used to account for the non-LTE assumption.

The optimized designs found by the algorithm shared similar features. For instance, the layers further from the heat-generating base were more porous than the ones closer to it. Moreover, all layers were attributed a pore diameter value close to the optimal value obtained from a numerical investigation. They were all essentially the same since the optimal value depends mainly on the Bejan number. As expected, the more the structure was constrained, i.e. the less freedom to morph it had, the highest was its hot spot temperature (Bejan and Lorente, 2004). The global mass and cost of each optimized constrained design closely satisfied the given constraints.

The size of the system had the possibility to be optimized as well. In fact, the GA could indirectly optimize the height of the stacked structure by removing layers, i.e. set $\phi = 1$ in that layer. This dimension optimization is the result of a competition between the different objectives considered (small mass and/or cost and low hot spot temperature).

In this study, we compared the hot spot temperature in the designs resulting from the optimizations (non-LTE) with the ones calculated if LTE is assumed (Wildi-Tremblay and Gosselin, 2007). Assuming LTE can result in underestimating the hot spot temperature or generate an erroneous ''optimal'' design, which could lead to system failures in practice. Therefore, it is preferable to let the GA chose whether LTE should be present or not instead of assuming it, i.e. to let the GA optimize the system in regard of the local thermal equilibrium as well as of the other design parameters. We can draw an analogy with Gosselin (2005, 2006) in which the flow regime was optimized rather than assumed in fluid networks and heat dissipation structures.

Since radiation effects become important in processes involving high temperatures (Al-Harbi, 2005) and that viscous dissipation can reduce significantly the convection heat transfer (Jiang and Ren, 2001), one could refine the analysis presented here by including these effects in the models. In further work, the optimal internal porous architecture of each layer could also be optimized. A database of various options (e.g., packed spheres, cylinders or tetrakaidecahedron, straight channels) and of their corresponding permeability–porosity and conductivity–porosity relations would then have to be created.

Acknowledgement

L. Gosselin's work was supported by the Natural Sciences and Engineering Research Council of Canada (NSERC).

References

Al-Harbi, S.M., 2005. Numerical study of natural convection heat transfer with variable viscosity and thermal radiation from a cone and wedge in porous media. Applied Mathematics and Computation 170, 64–75.

Amiri, A., Vafai, K., Kuzay, T.M., 1995. Effects of boundary conditions on non-Darcian heat transfer through porous media and experimental comparisons. Numerical Heat Transfer 27, 651–664.

Amiri, A., Vafai, K., 1994. Analysis of dispersion effects and non-thermal equilibrium, non-Darcian, variable porosity incompressible flow through porous media. International Journal of Heat and Mass Transfer 37, 939–954.

Bejan, A., 2000. Shape and Structure, From Engineering to Nature. Cambridge University Press, UK.

Bejan, A., 2004a. Designed porous media: maximal heat transfer density at decreasing length scales. International Journal of Heat and Mass Transfer 47 (14-16), 3073–3083.

Bejan, A., 2004b. Convection Heat Transfer, 3rd ed. Wiley, New York (Chapter 12).

Bejan, A., Lorente, S., 2004. The constructal law and the thermodynamics of flow system with configuration. International Journal of Heat and Mass Transfer 47 (14-16), 3203–3214.

Bobaru, F., Rachakonda, S., 2004. Optimal shape profiles for cooling fins of high and low conductivity. International Journal of Heat and Mass Transfer 47, 4953–4966.

Boomsma, K., Poulikakos, D., Ventikos, Y., 2003a. Simulations of flow through open cell metal foams using an idealized periodic cell structure. International Journal of Heat and Fluid Flow 24 (6), 825–834.

Boomsma, K., Poulikakos, D., Zwick, F., 2003b. Metal foams as compact high performance heat exchangers. Mechanics of Materials 35 (12), 1161–1176.

Boomsma, K., Poulikakos, D., 2001. On the effective thermal conductivity of a three-dimensionally structured fluid-saturated metal foam. International Journal of Heat and Mass Transfer 44 (4), 827–836.

Çengel, A., 2003. Heat Transfer: A Practical Approach, second ed. McGraw-Hill, New York.

Crittenden, P.E., Cole, K.D., 2005. Design of experiments for thermal characterization of metallic foam. Journal of Thermophysics and Heat Transfer 19 (3), 367–374.

Giani, L., Groppi, G., Tronconi, E., 2005. Heat transfer characterization of metallic foams. Industrial and Engineering Chemistry Research 44 (24), 9078–9085.

Gosselin, L., 2005. Minimum pumping power fluid tree networks without a priori flow regime assumption. International Journal of Heat and Mass Transfer 48 (11), 2159–2171.

Gosselin, L., 2006. Fitting the flow regime in the internal structure of heat transfer systems. International Communications in Heat and Mass Transfer 33 (1), 30–38.

Incropera, F.P., DeWitt, D.P., 2002. Fundamentals of Heat and Mass Transfer, fifth ed. Wiley.

Jany, P., Bejan, A., 1998. Ernst Schmidt's approach to fin optimization: an extension to fins with variable conductivity and the design of ducts for fluid. International Journal of Heat and Mass Transfer 31, 1635–1644.

Jeng, T.-M., Hwang, G.J., Hung, Y.H., 2001. Thermal performance of metallic porous channels for electronics cooling application. Advances in Electronic Packaging 2, 943–949.

Jeng, T.-M., Tzeng, S.-C., 2005. Numerical study of confined slot jet impinging on porous metallic foam heat sink. International Journal of Heat and Mass Transfer 48, 4685–4694.

Jiang, P.X., Ren, Z.P., Wang, B.X., 1999. Numerical simulation of forced convection heat transfer in porous plate channels using thermal equilibrium or non-thermal equilibrium models. Numerical Heat Transfer 35, 99–113.

Jiang, P.X., Ren, Z.-P., 2001. Numerical investigation of forced convection heat transfer in porous media using a thermal non-equilibrium model. International Journal of Heat and Fluid Flow 22, 102–110.

Khashan, S.A., Al-Amiri, A.M., Pop, I., 2006. Numerical simulation of natural convection heat transfer in a porous cavity heated from below using a non-Darcian and thermal non-equilibrium model. International Journal of Heat and Mass Transfer 49 (5–6), 1039–1049.

Lage, J.L., Weinert, A.K., Price, D.C., Weber, R.M., 1996. Numerical study of a low permeability microporous heat sink for cooling phased-array radar systems. International Journal of Heat and Mass Transfer 39 (17), 3633–3647.

Lee, D.Y., Vafai, K., 1999. Analytical characterization and conceptual assessment of solid and fluid temperature differences in porous media. International Journal of Heat and Mass Transfer 42, 423–435.

Mahfoud, S., 1995.Niching methods for genetic algorithms. ILLIGAL report 95001, University of Illinois at Urbana-Champaign.

Nield, D.A., Bejan, A., 1991. Convection in Porous Media. Springer-Verlag.

Patankar, S.V., 1980. Numerical Heat Transfer and Fluid Flow. Hemisphere.

Pham, D.C., Torquato, S., 2003. Strong-contrast expansions and approximations for the effective conductivity of isotropic multiphase composites. Journal of Applied Physics 94 (10), 6591–6602.

Renner, G., Ekárt, A., 2003. Genetic algorithms in computer aided design. Computer-Aided Design 35 (8), 709–726.

Tadrist, L., Miscevic, M., Rahli, O., Topin, F., 2004. About the use of fibrous materials in compact heat exchangers. Experimental Thermal and Fluid Science 28 (2-3), 193–199.

Wildi-Tremblay, P., Gosselin, L., 2007. Layered Porous Media Architecture for Maximal Cooling. International Journal of Heat and Mass Transfer 50 (3–4), 464–478.

www.metalprices.com, (26.10.2005).